

Intravascular Ultrasound Image Segmentation: A Three-Dimensional Fast-Marching Method Based on Gray Level Distributions

Marie-Hélène Roy Cardinal, Jean Meunier, Gilles Soulez, Roch L. Maurice, Éric Therasse, and Guy Cloutier*

Abstract—Intravascular ultrasound (IVUS) is a catheter based medical imaging technique particularly useful for studying atherosclerotic disease. It produces cross-sectional images of blood vessels that provide quantitative assessment of the vascular wall, information about the nature of atherosclerotic lesions as well as plaque shape and size. Automatic processing of large IVUS data sets represents an important challenge due to ultrasound speckle, catheter artifacts or calcification shadows. A new three-dimensional (3-D) IVUS segmentation model, that is based on the fast-marching method and uses gray level probability density functions (PDFs) of the vessel wall structures, was developed. The gray level distribution of the whole IVUS pullback was modeled with a mixture of Rayleigh PDFs. With multiple interface fast-marching segmentation, the lumen, intima plus plaque structure, and media layers of the vessel wall were computed simultaneously. The PDF-based fast-marching was applied to 9 *in vivo* IVUS pullbacks of superficial femoral arteries and to a simulated IVUS pullback. Accurate results were obtained on simulated data with average point to point distances between detected vessel wall borders and ground truth <0.072 mm. On *in vivo* IVUS, a good overall performance was obtained with average distance between segmentation results and manually traced contours <0.16 mm. Moreover, the worst point to point variation between detected and manually traced contours stayed low with Hausdorff distances <0.40 mm, indicating a good performance in regions lacking information or containing artifacts. In conclusion, segmentation results demonstrated the potential of gray level PDF and fast-marching methods in 3-D IVUS image processing.

Index Terms—Fast-marching, IVUS, probability density function, segmentation, 3-D imaging.

Manuscript received November 21, 2005; revised January 16, 2006. This work was supported in part by the Canadian Institute of Health Research under Grant MOP-53244 and in part by Valorisation-Recherche Québec under Grant 2200-094. The work of M. H. Roy Cardinal was supported in part by a studentship award from the Fonds de la Recherche en Santé du Québec and the Groupe de modélisation biomédicale of the Institute of biomedical engineering of the University of Montreal. The work of G. Soulez was supported in part by the Fonds de la Recherche en Santé du Québec under a clinical scholarship. The work of G. Cloutier was supported in part by Fonds de la Recherche en Santé du Québec under a National Scientist award.

M.-H. Roy Cardinal and R. L. Maurice are with the Laboratory of Biorheology and Medical Ultrasonics, University of Montreal Hospital's Research Center, 2099 Alexandre de Séve, Montréal, QC H2L 2W5, Canada (e-mail: roy-carmh@iro.umontreal.ca).

J. Meunier is with the Département d'Informatique et de Recherche Opérationnelle, University of Montreal, Montréal, QC H3A 2B2, Canada.

G. Soulez and É. Therasse are with the Radiology Department, University of Montreal Hospital, Montréal, QC H2L 2W5, Canada.

*G. Cloutier is with the Laboratory of Biorheology and Medical Ultrasonics, University of Montreal Hospital's Research Center, Montréal, QC H2L 2W5, Canada (e-mail: guy.cloutier@umontreal.ca).

Digital Object Identifier 10.1109/TMI.2006.872142

I. INTRODUCTION

OVER the past few years, intravascular ultrasound (IVUS) technology has become very useful for studying atherosclerotic disease. IVUS is a medical imaging technique that produces cross-sectional images as a catheter is pulled-back inside blood vessels. These images show the lumen but also the layered structure of the vascular wall. It provides quantitative assessment of the wall, information about the nature of atherosclerotic lesions as well as the plaque shape and size. In clinic, IVUS was rapidly recognized as a valuable tool in diagnosis and in pre-intervention analysis of atherosclerosis. Its ability to characterize the vascular wall was initially proven in 1989 [1] and studies of the mid-1990s showed *in vivo*, based on IVUS images, that 40% of angiographically normal vessels were in fact atherosclerotic [2]. It may be worth mentioning that this phenomenon, known as compensatory arterial enlargement, had been earlier observed on histologic cuts [3]. It was also demonstrated, using IVUS, that conventional stent implantation resulted in incomplete apposition and expansion causing thrombosis, which changed the clinical practice [4]. IVUS is also expected to play an important role in atherosclerosis research; for example, to achieve precise evaluation of the disease in new progression-regression therapies [5]. Experts agree that IVUS imaging adds precious complementary information to angiography which only shows a projection of the lumen [6].

The tomographic nature of IVUS makes three-dimensional (3-D) reconstruction of the vessel wall possible. When combined to biplane angiography to recover the catheter path, geometrically accurate 3-D reconstruction is also feasible [7], [8]. Furthermore, two-dimensional (2-D) and 3-D quantitative measurements of atherosclerotic disease such as plaque volume, intima-media thickness, vascular remodeling and lumen area stenosis can be retrieved from IVUS data [9]. However, a typical IVUS acquisition contains several hundred of images making nonautomatic analysis of the data long, fastidious and subject to intraobserver and interobserver variabilities. These could be serious constraints against the clinical usage of IVUS. In addition, because IVUS image quality remains poor due to speckle noise, imaging artifacts and shadowing of parts of the vessel wall by calcifications, it is necessary to develop specific segmentation methods that take into account the nature of IVUS images.

So far, a number of segmentation techniques have been developed for IVUS data analysis. A great portion of this work was based on local properties of image pixels, namely gradient-based active surfaces [10] and pixel intensity combined to

gradient active contours [11]. Graph search was also investigated using local pixel features: e.g., Sobel-like edge operator [12] and gradient associated to line patterns correlation [13]. Another portion of the IVUS segmentation work was based on more global or region information. Texture-based morphological processing was considered [14]. Gray level variances were then used for the optimization of a maximum *a posteriori* (MAP) estimator modeling ultrasound speckle and contour geometry [15]. In addition, some studies defining only the lumen boundary and not using the full IVUS potential can be found in the literature. Still, in 2001, a clinical expert consensus from the American College of Cardiology [9] reported that no IVUS edge detection method had found widespread acceptance by clinicians.

Recently, graph search was revisited using other edge filters [16]. Hereafter, other methods such as elliptical template fitting [17] and multiagent segmentation [18] were proposed. However, these new models were again using local pixel or edge information and they were not taking advantage of the statistical information of IVUS data (speckle texture). Very recently, the MAP estimator was revised using statistics of the signal [19], but for the lumen contour only and without modeling of the whole IVUS graylevel statistical distribution.

The aim of this paper was, thus, to achieve IVUS image segmentation by using global image features and a region based model. Since pixel gray values are distributed according to a Rayleigh probability density function (PDF) in B-mode imaging of uniform scattering tissues [20], [21], it is believed that PDF features can be of value for IVUS segmentation. This information is hypothetically valuable for IVUS image analysis, especially when the vascular wall edges are weakly defined.

The atherosclerotic plaque structure can have an irregular and complex shape that is rarely elliptical. A fast-marching method [22], derived from the level-set model, that can handle topological changes and object irregularities should, therefore, be appropriate for IVUS images. Also, fast-marching propagates interfaces in the direction of the boundaries through an exhaustive analysis of the propagation region, this should decrease the variability of segmentation results. Consequently, this paper proposes a 3-D fast-marching segmentation based on automatic detection of vessel wall component PDFs to address the IVUS segmentation problem.¹ The fast-marching combined to gray level gradient was also evaluated for comparison purpose.

The paper is organized as follows: Section II presents the PDF estimation algorithm of the different vessel wall structures. The IVUS 3-D fast-marching method based on estimated PDFs and gray level gradient is detailed in Section III followed by the initialization technique. Experimental and simulated data are presented in Sections IV and V. Segmentation results are then reported in Section VI and discussed in Section VII.

II. PROBABILITY DENSITY FUNCTION ESTIMATION

In B-mode imaging,² a Rayleigh PDF can model the gray level distribution of the ultrasonic speckle pattern in a uniform

scattering tissue [21]. The gray level distribution of a whole IVUS series can then be estimated by a mixture of Rayleigh PDFs, each corresponding to the lumen, plaque structure of the intima, media, and adventitia plus surrounding tissues.

The expectation-maximization algorithm (EM) is an iterative computation technique of maximum likelihood estimates for incomplete data [24]. It provides the parameters of a density distribution function in which information is hidden. In IVUS imaging, the occurring probability of the gray level values, or observed data, can be measured by computing the image histogram. But the vessel wall structure to which each pixel belongs is unknown or hidden for images that are not segmented. Because the IVUS data are incomplete in terms of maximum likelihood estimation, the EM algorithm was applied to evaluate the mixture parameters.

The Rayleigh PDF $p_X(x)$ with parameter a^2 , where X is the gray level taking values in $[1, \dots, 256]$, is given by

$$p_X(x; a^2) = \frac{x}{a^2} \exp\left(-\frac{x^2}{2a^2}\right) \quad (1)$$

with $x, a^2 > 0$ and the variance $\sigma^2 = a^2(4 - \pi)/2$.

IVUS data, in which there are M different tissue structures, were modeled by a mixture of M Rayleigh PDFs with parameters $\Theta = \{(\omega_j, a_j^2)\}_{j=1}^M$, where ω_j is the proportion of the j th component of the mixture so that $\sum_{j=1}^M \omega_j = 1$. The PDF mixture then becomes

$$p_{X|\Theta}(x|\Theta) = \sum_{j=1}^M \omega_j p(x|a_j^2). \quad (2)$$

To describe the global data PDF, the parameters (ω_j, a_j^2) of each distribution composing the mixture need to be estimated. The EM algorithm is necessary because $\hat{\Theta}$, the mixture parameter maximizing the likelihood of $p(X|\Theta)$, cannot be solved analytically. A hidden variable Y , the tissue class taking values $[1, \dots, M]$, must be introduced at this point. The log-likelihood of the joint distribution of $(X, Y) = \{(x_i, y_i)\}_{i=1}^N$, where N is the data size, is

$$\log(p_{X,Y|\Theta}(x, y|\Theta)) = \sum_{i=1}^N \log p(y_i) p(x_i|y_i, \Theta). \quad (3)$$

The first step of the EM algorithm (Expectation) is the calculation of the cost function $Q(\Theta, \Theta') = E_Y[\log(P(X, Y|\Theta))|X, \Theta']$, the expected value of the log-likelihood of (X, Y) , the joint distribution, given the observed data X and $\Theta' = \{(\omega'_j, a'^2_j)\}_{j=1}^M$, a previous estimate of the mixture parameters. The next step is to evaluate $\hat{\Theta}$, the new parameter estimate, by maximizing $Q(\Theta, \Theta')$ with respect to Θ , that can now be done analytically.

The detailed PDF parameter estimation procedure via the EM algorithm is as follows.

- Initialize Θ' , the previous estimate of mixture parameters.³

¹A preliminary 2-D version of this paper can be found in [23].

²The B-mode signal is the envelop filtered radio-frequency signal.

³Initialize $\omega'_j = (1/M) +$ random value between $-1/M$ and $1/M$ with $\omega'_M = 1 - \sum_{j=1}^{M-1} \omega'_j$, and $a'^2_j =$ random value between 1 and $2\sigma^2/(4 - \pi)$, where σ^2 is the variance of the pixel gray values.

TABLE I
ESTIMATED PROBABILITY DENSITY FUNCTION PARAMETERS FOR 30 RUNS OF
THE EM ALGORITHM ON 1 IVUS PULLBACK

Component	ω (%)	a^2
Lumen	29.63±0.88	0.6456±0.0014
Intima and Plaque	20.72±0.72	341.53±6.49
Media	13.49±0.11	22.43±0.39
Surrounding Tissues	36.19±0.24	2283.04±12.09

- Expectation:
Evaluate the cost function

$$Q(\Theta, \Theta') = E_Y [\log(P(X, Y|\Theta)) | X, \Theta'] \quad (4)$$

$$= \sum_{j=1}^M \sum_{i=1}^N \log(\omega_j p(x_i | a_j^2) p(y_i = j | x_i, \Theta')). \quad (5)$$

Calculate $p(y_i = j | x_i, \Theta') = (\omega'_j p(x_i | a_j'^2) / \sum_{k=1}^M \omega'_k p(x_i | a_k'^2))$, according to Bayes rule, and using the previous parameter estimate Θ' and (1).

- Maximization:
Calculate $\hat{\Theta}$, the new estimate of the mixture parameters

$$\hat{\omega}_j = \underset{\omega_j}{\operatorname{argmax}} \left(Q(\Theta, \Theta') + \lambda \left(1 - \sum_{j=1}^M \omega_j \right) \right) \\ = \frac{1}{N} \sum_{i=1}^N p(y_i = j | x_i, \Theta') \quad (6)$$

where $\lambda = N$ is a Lagrangian making the ω_j sum to 1.

$$\hat{a}_j^2 = \underset{a_j^2}{\operatorname{argmax}} Q(\Theta, \Theta') \\ \hat{a}_j^2 = \frac{\sum_{i=1}^N p(y_i = j | x_i, \Theta') x_i^2}{2 \sum_{i=1}^N p(y_i = j | x_i, \Theta')} \quad (7)$$

- If $\hat{\Theta} \neq \Theta'$, update previous estimate $\Theta' = \hat{\Theta}$, repeat expectation/maximization.

In summary, the EM algorithm maximizes the likelihood of the joint distribution of the observed and hidden data by estimating the posterior distribution with $p_{Y|X, \Theta'}(y|x, \Theta')$. An interesting property of the EM algorithm is that it is guaranteed that the likelihood of the observed data X increases at each iteration [24].

For computation efficiency, the EM algorithm was only applied to a randomly drawn subset of the observed data X , which are, in this case, pixels from the whole IVUS series. The subset size was about 400 000 pixels, a complete IVUS pullback contained over 80 000 000 pixels. It is to note that no statistically significant difference was found between the parameters calculated for a subset of this size and the whole observed data set ($p > 0.2$ for each parameter on the effect of subsampling according to two-way ANOVA tests⁴ on parameters calculated from 5 whole IVUS series and 30 different subsets for each pullback). The subset pixels were randomly sampled from axial IVUS frames of the whole pullback. An example of average mixture parameters for runs of the EM algorithm on 30 different subsets from 1 IVUS pullback is shown in Table I described in Section VI.

⁴SPSS statistical software, version 13.0, SPSS Inc., Chicago, IL.

Once the gray level distributions of the artery components were estimated, they were used as segmentation features.

III. SEGMENTATION MODEL

A. Fast-Marching Method

The fast-marching method was derived from the level-set model introduced by Osher and Sethian to follow an interface (or front, or contour) propagating under a speed function F [22], [25]. These methods can be applied to image segmentation by interpreting an image boundary as the propagating interface final position [22], [26]. To achieve this, the speed function is defined in terms of image or shape features and should become close to zero when the propagating front meets with object borders. The interface stop on image boundaries since the speed value is near zero, which ends the segmentation process.

Fast-marching is a particular case of the level-set model. It consists of the evolution of an interface propagating under a unidirectional speed function. In this case, the evolving contour must be inside the region to segment (for a positive speed function or outside for a negative one) because the front does not explore its initial inside region. In the fast-marching formulation, the evolution of the contour is expressed in terms of the arrival time $T(x)$ of the contour at point $x = (x_1, x_2, \dots, x_n) \in \mathbb{R}^n$. The T function satisfies (8), stating that the arrival time difference between two adjacent pixels increases as the velocity of the contour decreases

$$|\nabla T|F = 1. \quad (8)$$

The propagation of the interface is done via the construction of the arrival time function. The construction algorithm [27] selects the interface point having the smallest arrival time and calculates the arrival times of its neighbors. This is repeated until the interface has propagated across the whole image or until the front is considered stationary (when the time gradient is sufficiently high). The fast-marching equation is independent of the interface dimension. On a discrete 3-D grid, neighbors' arrival times are updated by solving (9) [22], an approximation of (8). Another method, proposed in [28], can be used to solve (8)

$$\frac{1}{F_{i,j,k}^2} = \max \left(D_{i,j,k}^{-x} T, -D_{i,j,k}^{+x} T, 0 \right)^2 \\ + \max \left(D_{i,j,k}^{-y} T, -D_{i,j,k}^{+y} T, 0 \right)^2 \\ + \max \left(D_{i,j,k}^{-z} T, -D_{i,j,k}^{+z} T, 0 \right)^2. \quad (9)$$

For the x dimension

$$D_{i,j,k}^{\pm x} T = \pm \frac{(T_{i\pm 1,j,k} - T_{i,j,k})}{\Delta}$$

where Δ is the grid element size and (i, j, k) is the 3-D position of the point having its arrival time calculated. Similar definitions apply for $D_{i,j,k}^{\pm y} T$ and $D_{i,j,k}^{\pm z} T$, in the y and z dimensions.

Since multiple borders (lumen, intima and media) must be identified on the IVUS series, image segmentation is done via

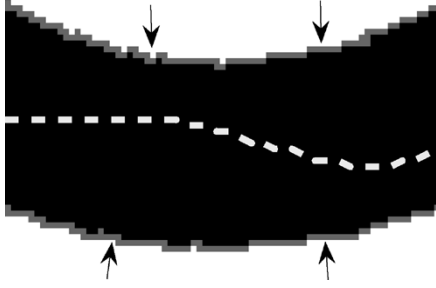


Fig. 1. Example of two interfaces propagating in opposite directions to detect a boundary. The black region is the unexplored propagation area. The white dashed line is the desired boundary. The gray pixels on each side of the black region correspond to the propagating interfaces that will meet at the boundary; the arrows indicate the direction of propagation.

a multiple interface extension of the fast-marching algorithm [29]. For this particular case, a boundary is defined by the meeting position of two contours propagating in opposite directions. Fig. 1 shows a schematic representation of the multiple interface fast-marching for the detection of a boundary in which the interfaces propagating in opposite directions are represented by the gray lines on each side of the propagation area that is represented by the black region. Fig. 1 also shows that each interface propagates inside the region that it segments. A speed function must then be determined for each propagating interface and the T map is built by selecting the point with the smallest arrival time value from all interfaces.⁵ Notice that the multiple interface fast-marching enables simultaneous segmentation of different parts of the vessel wall. The multiple interfaces directly depict the layered structure of the wall and prevent the detected borders from overlapping.

In the PDF-based fast-marching, each interface propagating in a vessel wall layer evolves at a velocity defined in terms of the PDF $P_{m \in L}$ of the corresponding anatomical structure. The propagation speed of interface $m \in L$, where L is the set $1, 2, \dots, N_L$ of the N_L vessel wall structures, is given by (10)

$$F_m(i, j, k) = \left(1 + \frac{1}{N_v} \sum_{s \in \nu} \frac{\log P_m(I_s)}{\frac{1}{N_L - 1} \sum_{l \neq m, l \in L} \log P_l(I_s)} \right)^{-1}. \quad (10)$$

I_s is the gray level value of pixel s at position (i, j, k) in image I , $P_m(I_s)$ and $P_l(I_s)$ are the measured occurring probabilities of pixel I_s in region m and l . Because the occurring probability is more significant for a region than for a single pixel, the speed function is calculated over a certain number N_v of neighbors, which are the 26-connected pixels around (i, j, k) . According to (10), the interface m velocity will always be positive and will take higher values when inside a region having a grayscale distribution close to P_m . As the front approaches the boundary, neighbors start to be distributed under other component PDFs, this should increase $P_l(I_s)$, decrease $P_m(I_s)$ and the interface speed. This velocity function has a general form that can be used with any types of PDF and provides neighborhood averaging.

⁵A detailed description of the T map construction algorithm can be found in [29].

Since gray level gradient is a widely accepted image feature, comparison was also made with a gradient implementation of the fast-marching segmentation. The speed function is given by [22]:

$$F(i, j, k) = \frac{1}{1 + |\nabla G_\sigma * I_s|} \quad (11)$$

where G_σ is a 9×9 pixel symmetric gaussian smoothing filter of standard deviation $\sigma = 0.5$ and the gradient is computed in 2-D. This speed function propagates interfaces faster on low gradient regions.

Multiple interface fast-marching segmentation is finished when all fronts propagating in opposite directions have met. Fronts are, thus, obligated to evolve until the arrival time map is completely built.

B. Segmentation Initialization

This fast-marching segmentation requires the initial interfaces propagating in opposite directions to include the border of the object to segment. This was assured with an initialization procedure in which propagation regions were computed; the initial interfaces propagating in opposite directions were set as the bounding contours of the propagation region (see Fig. 1). The initial regions were determined from manually traced contours on longitudinal images (L-views) of the IVUS series. Longitudinal cuts of the IVUS volume were used, instead of a single 2-D IVUS frame, because they give information about the whole series. Also, the number of manually traced contours on longitudinal images is independent of the number of IVUS 2-D slices.

On each longitudinal view and on both sides of the catheter [see Fig. 2(a)], a contour was traced close to the lumen boundary and another one inside the media (which appears as a hypoechoic ring on axial frames). Contours from three different longitudinal cut planes at equally spaced angles over 360 degrees were sufficient to compute the initial propagation areas. The number of planes was not fixed, although 3 seemed to be adequate in the current study; it had to be chosen so that the vessel wall boundaries were included in the propagation regions. At the end of this procedure, 4 lines were traced on 3 longitudinal images (for a total of 6 points on the lumen border and 6 points inside the media in each axial frame).

The longitudinal contour points were spline-interpolated axially and longitudinally while being forbidden to overlap (to preserve the layered structure of the vessel wall). The axial lumen contours were then shifted radially in the 2 opposite directions to compute the pair of 3-D tube-like initial lumen interfaces, as illustrated by the gray lines on Fig. 1. The axial contours inside the media were used to compute 2 pairs of interfaces to initialize the segmentation of the internal and external media boundaries.⁶ The first pair of interfaces, to initialize the inner media border, was composed of the axial contours inside the media and of an inward radially shifted version of these contours. The pair of

⁶The internal media border delimits the plaque of the intima, whereas the external media border separates the external tissue from the vessel wall.

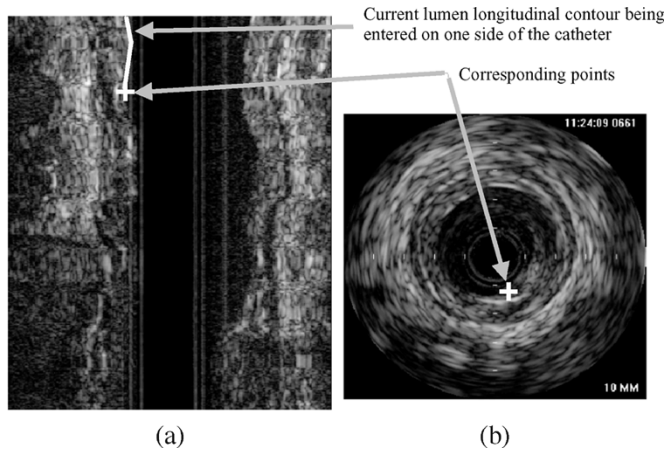


Fig. 2. (a) Longitudinal IVUS image of the 3-D data set in which a contour is being entered and (b) current longitudinal contour point displayed on the corresponding 2-D IVUS image. At the end of the initialization procedure, 4 lines were traced in 3 longitudinal images (that converts into 6 points on the lumen border and 6 points inside the media in each axial frame).

outer media border initial interfaces was set similarly, but with an outward radial shift of the axial media contours. The length of the radial shifts were set to separate the interfaces of each pair (lumen, inner and outer media) by 24 pixels (0.625 mm). These 3 propagation regions, when combined, corresponded to $55 \pm 5\%$ of the vessel volume. More than half of the vessel volume was, thus, explored with the propagating interfaces.

To facilitate interaction, the last longitudinal point clicked by the user was displayed on the corresponding IVUS frame as shown by Fig. 2. The contour could also be restarted from any previous points. This way, the user could explore, on-line and easily, sections of an IVUS series that were more difficult to interpret on L-views.

IV. EXPERIMENTAL DATA

A total of 9 *in vivo* IVUS pullbacks (of 600 frames/series) from diseased superficial femoral arteries of either one or both legs were performed on 7 patients before undergoing balloon angioplasty. In these cases where the disease is advanced, the vessels reveal extensive irregular atheromas that project into the lumen [30]. Data were acquired with a Jomed equipment (In-vision gold, Helsingborg, Sweden) using a 20-MHz transducer. Images of size 10×10 mm were digitized on 384×384 pixel matrices and stored using the DICOM standard. The acquisition was done at a 10 images/sec frame rate and the catheter pullback velocity was set to 1 mm/sec generating 0.1 mm thick 2-D slices. Acquisition parameters were set by the clinician to optimize image quality (the gain varied from 46 to 54 and the grayscale look-up table was set to 5). Image acquisition was not ECG-gated.

A. Validation

The EM algorithm was applied at the beginning of each segmentation because mixture parameters are specific to each IVUS series as gain and other parameter settings were different and the echogenicity of the different wall components was variable between patients. The detected mixtures were composed of 4 distributions (corresponding to the lumen, intima,

media, and surrounding tissues regions). Each pullback was, thus, segmented with its own set of parameters. The IVUS series were segmented three times with both 3-D methods using different sets of initial fronts. Lumen, intima (plaque), and media borders were obtained.

To validate the segmentation results, comparison was made with manually drawn contours. Boundaries were traced two times by two independent experimented users (Z. Qin. and I. Renaud) on 1 every 10 frames of each IVUS pullback. For each series, boundary positions from 60 IVUS frames were, thus, available. Even though 3 contours were available with the fast-marching segmentation, the validation was performed only on the lumen and external media boundaries. For instance, it is not the practice to manually trace the intima-media boundary because, in any artery IVUS scans, this boundary is not well delineated as pointed out by the IVUS clinical expert consensus [9]. The consensus, thus, established that plaque measurements should be made with the lumen and the external media borders.

To quantify the boundary detection accuracy, average and Hausdorff point to point distances [31], and area differences between the manually traced contours and segmentation results were calculated. Hausdorff distance represents the worst case, it is the maximum distance between different contours. Average and Hausdorff distances directly depict point to point contour variations. Since each pullback was manually analyzed four times (two times per user expert), the error metrics were also calculated between the different manually traced contours to evaluate the intrauser and interuser variabilities.

Moreover, to quantify the repeatability of the segmentation results under various initializations, average and Hausdorff point to point distances between segmentation results from different initial contour sets were calculated.

Detected boundaries from a whole IVUS pullback represent the wall layers in 3-D without the vessel curvature. Reconstruction of the vessel boundaries was made from a simple smoothed contour stack (see Fig. 8, Section VI).

B. Statistical Analysis

Multiple pairwise comparisons with Bonferonni tests were performed for the average and Hausdorff distances, and area differences. The analysis was carried out on metrics calculated with the manual and 3-D fast-marching contours based on PDF and gradient features; the same statistical test was also used to assess the significance of the distance metrics and area differences with respect to the intrauser and interuser variabilities. The average and Hausdorff distances between segmentation results from each method for different initial contour sets were compared with paired t-tests. All statistical analyses were performed with the SPSS statistical software, version 13.0, SPSS Inc., Chicago, IL.

V. NUMERICAL SIMULATION OF IVUS DATA

In addition to the above validation of the segmentation methods, realistic simulations of IVUS data were conducted to evaluate the segmentation accuracy. Since the exact geometry of simulated data is known, direct calculation of the detected boundary performance could be obtained. The simulated IVUS images were segmented using the same algorithms as for the *in*

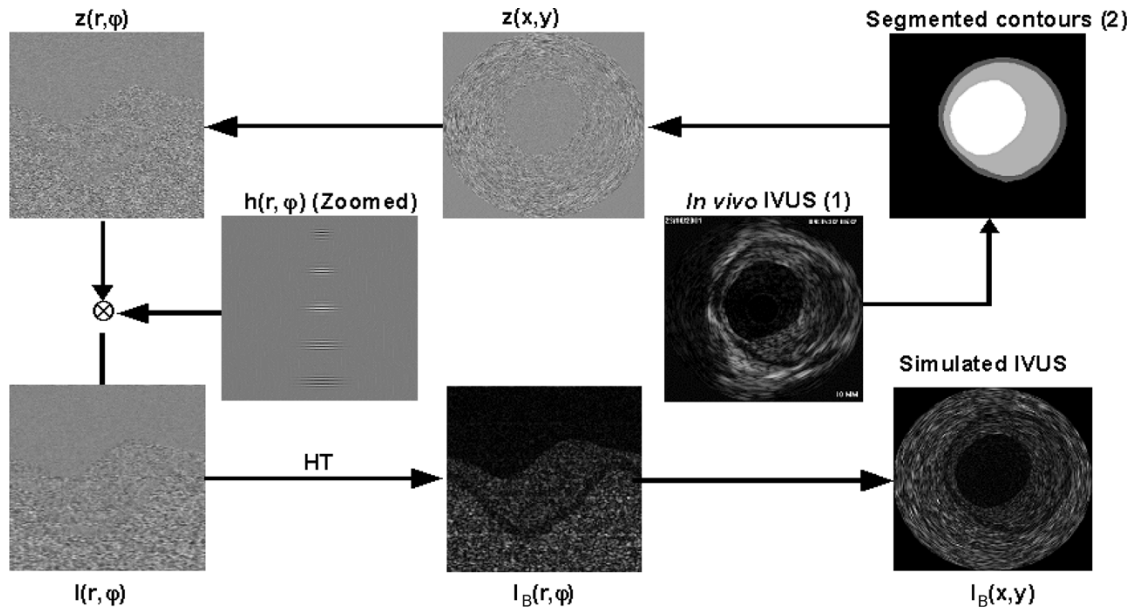


Fig. 3. Schematic implementation of the image-formation model. An *in vivo* IVUS pullback (1) was used to create the vessel geometry (2). $z(x, y)$ is a function representing the acoustic impedance variations; $z(r, \varphi)$ is the acoustic impedance function mapped in polar coordinates; $h(r, \varphi)$ is the polar PSF, with a beam width that increases with depth; \otimes is the 2-D-convolution operator; $I(r, \varphi)$ is the simulated polar radio-frequency image; $I_B(r, \varphi)$ is the polar B-mode image, that was computed using the Hilbert transform (HT) [33] of $I(r, \varphi)$; $I_B(x, y)$ is the Cartesian B-mode image or simulated IVUS image. This simulation strategy was repeated for the whole image series of a pullback within a diseased superficial femoral artery. For more details on the simulation model, refer to [32].

in vivo data, also with 3 different sets of initial L-view contours. Lumen, intima (plaque), and media borders were obtained. Average and Hausdorff point to point distances between ground truth and detected boundaries were calculated for segmentation results from each set of initial contours.

The image-formation model that was used to simulate the IVUS echograms is detailed in [32]. Under assumptions such as space-invariance of the imaging system, IVUS images were modeled by a convolution operation between the point-spread function (PSF)⁷ of the ultrasound system and a function representing acoustic impedance variations within the vascular wall. The PSF was modeled by a one-dimensional cosine modulated by a 2-D Gaussian envelope: a simple approximation of the ultrasound far field PSF. One *in vivo* IVUS series was used to generate a realistic vessel geometry. The vessel boundaries (lumen, plaque of the intima, media) were created from manually traced contours, on longitudinal cuts of the IVUS data. The simulated pullback from a diseased superficial femoral artery (different from the 9 pullbacks described in Section IV) contained 86 IVUS 2-D frames.

Fig. 3 illustrates the implementation of the image-formation model for a 20-MHz transducer with a 60% bandwidth at -3 dB and a beam width of 0.1 mm. For the purpose of these simulations, the media was selected 2 times more echogenic than the lumen; the plaque, 1.5 times more echogenic than the media; and the surrounding tissues 2 times more echogenic than the media. The signal-to-noise ratio was set at 20 dB. For each vessel section, the scatterers were randomly positioned in space, and their backscattering cross-sections (echogenicity) were distributed according to a Gaussian model (with a standard deviation of 0.5).

⁷The PSF is the equivalent radio-frequency image of a single ultrasound scatterer. In other words, the PSF expresses the intrinsic characteristics of the ultrasound imaging system.

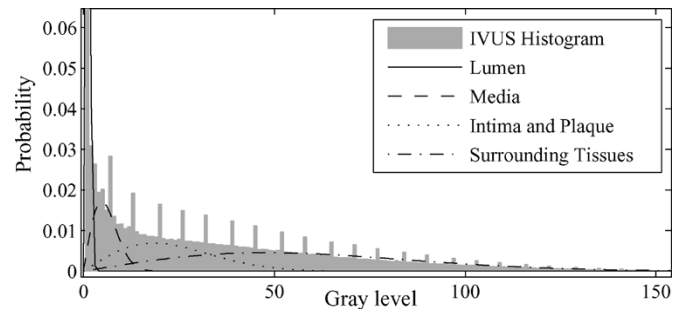


Fig. 4. Intravascular ultrasound image gray level histogram and detected mixture of PDFs.

A. Statistical Analysis

The average and Hausdorff distances between ground truth geometry and segmentation results from each method were compared with paired t-tests.

VI. RESULTS

A. Probability Density Function Estimation

An example of average mixture parameters detected with the EM algorithm on 30 different subsets from 1 IVUS pullback is shown in Table I. An automatically detected Rayleigh PDF mixture and corresponding IVUS pullback histogram is shown in Fig. 4. In the PDF mixture of Fig. 4, distribution overlaps occur for nonadjacent wall layers (the lumen and media; the plaque and the surrounding tissues); thus, the overlaps did not affect significantly the boundary detection process.⁸ The presence of regularly spaced histogram peaks, that are probably caused by

⁸The neighborhood averaging in (10) also gives additional information if gray values fall in the overlapping regions.

TABLE II
ESTIMATED PROBABILITY DENSITY FUNCTION PARAMETERS WITH THE EM
ALGORITHM, AVERAGE VALUES FOR THE 9 IVUS PULLBACKS

Component	ω (%)	a^2
Lumen	18.82±10.44	5.52±12.50
Intima and Plaque	27.81±14.54	1052.40±1405.97
Media	15.87±3.61	339.46±817.80
Surrounding Tissues	37.50±13.82	2580.49±654.49

a digitization artifact of the IVUS system, did not seem to interfere either with the parameter estimation.

Table I shows that small variations were found between different runs of the EM algorithm, it was, thus, applied to the 9 available pullbacks to study PDF variability between different patients. The results are shown in Table II.

B. Segmentation

1) *Simulated IVUS Data:* Typical results on simulated IVUS data for each method are displayed in Fig. 5. Table III shows the average and Hausdorff distances in mm between detected boundaries from different initializations and ground truth values obtained from the simulated geometry. Smaller average and Hausdorff distances were achieved with the gradient method on detected lumen borders. However, PDF feature had better worst case performance (Hausdorff distance) on plaque and media borders.

2) *In-vivo IVUS Data:* A typical segmentation result for the 3-D fast-marching method using PDFs and gradient is shown in Fig. 6. The lumen, intima and media detected boundaries are presented for 3 different cross-sectional IVUS images. A qualitative analysis of the PDF- and gradient-based fast-marching segmentation revealed detected contours that were very close to all vessel layers. An example of the PDF-based speed function calculated according to (10) for the lumen region is shown in Fig. 7 where the darker pixels depict lower speed values.

Table IV shows the average and Hausdorff distances, and area differences between the manually traced and detected boundaries. Table IV also presents the interuser and intrauser variabilities. Except for the media Hausdorff distance, statistically significant smaller average and Hausdorff distances, and area differences were obtained with both PDF- and gradient-based 3-D fast-marching methods when compared to the interuser variability. Area differences smaller than the intrauser variability were also achieved with both segmentation methods.

Table V shows average and Hausdorff distances between segmentation results from each method for different initial contour sets. Statistically significant better consistency was achieved with the PDF-based method for the worst case index on all vessel wall layers (smaller Hausdorff distances). Nevertheless, gradient-based segmentation presented lower variations on average distance for the media boundaries.

Fig. 8 shows a 3-D reconstruction of the lumen and media borders obtained with PDF-based 3-D fast-marching segmentation for which a double stenosis is clearly seen. The gradient fast-marching method provided similar qualitative results (data not shown).

VII. DISCUSSION

The goal of this paper was to demonstrate the IVUS segmentation potential of the 3-D fast-marching method, and the usefulness of region statistics (PDFs) in the determination of the vessel wall anatomical structures.

The EM algorithm was first presented to detect a mixture of Rayleigh distributions in IVUS data. Table I showed that mixture detection is a robust and stable process with standard deviations of ω and a^2 going from 0.2% to 3.5% for several runs of the algorithm on different pixel subsets of an IVUS pullback. As expected, because of instrument settings and echogenicities specific to the different plaque structures, Table II emphasized the high variability between mixture parameters of distinct pullbacks. These results suggest that the EM algorithm is capable of fitting various Rayleigh mixtures from different patients.

A. Comparison of the Segmentation Methods

The typical simulated IVUS segmentation results in Fig. 5 showed that detected boundaries were very close to the vessel wall structures. They also revealed that the external border of the media was smoother with the PDF fast-marching than with the gradient-based method, but that the lumen, which can have a rougher surface, was detected with sufficient details. Gradient methods seemed to trace speckle contours on objects' boundaries, because speckles have high gray level intensity differences.

As presented in Tables III–V, the average and Hausdorff distances were chosen as comparison metrics because they directly depict point to point contour variations. For the segmentation accuracy evaluation on simulated IVUS data, correlation coefficients between area measurements from simulated vessel and segmentation results were higher than 0.99 for both gradient and PDFs on each vessel layer. The average and Hausdorff distance are, thus, more sensitive metrics on simulated data. As seen in Table III, very low average and Hausdorff distance values were obtained, for both PDF- and gradient-based 3-D fast-marching, demonstrating that this method is very powerful for simulated IVUS segmentation. In fact, average deviation ranged from 0.060 to 0.072 mm and worst point to point distances were between 0.154 and 0.226 mm, which is highly satisfying. Lower Hausdorff distances were obtained on lumen boundary with the gradient method ($p < 0.01$) because the blood and intima frontier produces bright echoes for which the gradient information is significant. However, on less contrasting boundaries such as the intima (plaque) and media, statistically significant lower Hausdorff distances ($p < 0.05$) were achieved with the PDF-based method.

Fig. 6 showed that vessel wall boundaries of *in vivo* IVUS images could be identified even if the contrast was very low, as seen at 4 o'clock for the collateral vessel in Fig. 6(a) or behind a calcified plaque at 11 o'clock in Fig. 6(c). Also, boundaries in Fig. 6(e) and (h) demonstrated that noncircular lumen could be detected with fast-marching methods.

Fig. 7 was given as an example of a PDF-based speed function for one of the vessel wall structure (each layer has its own PDF speed function). The speed function map of the lumen region in Fig. 7 showed that the speed values calculated according to

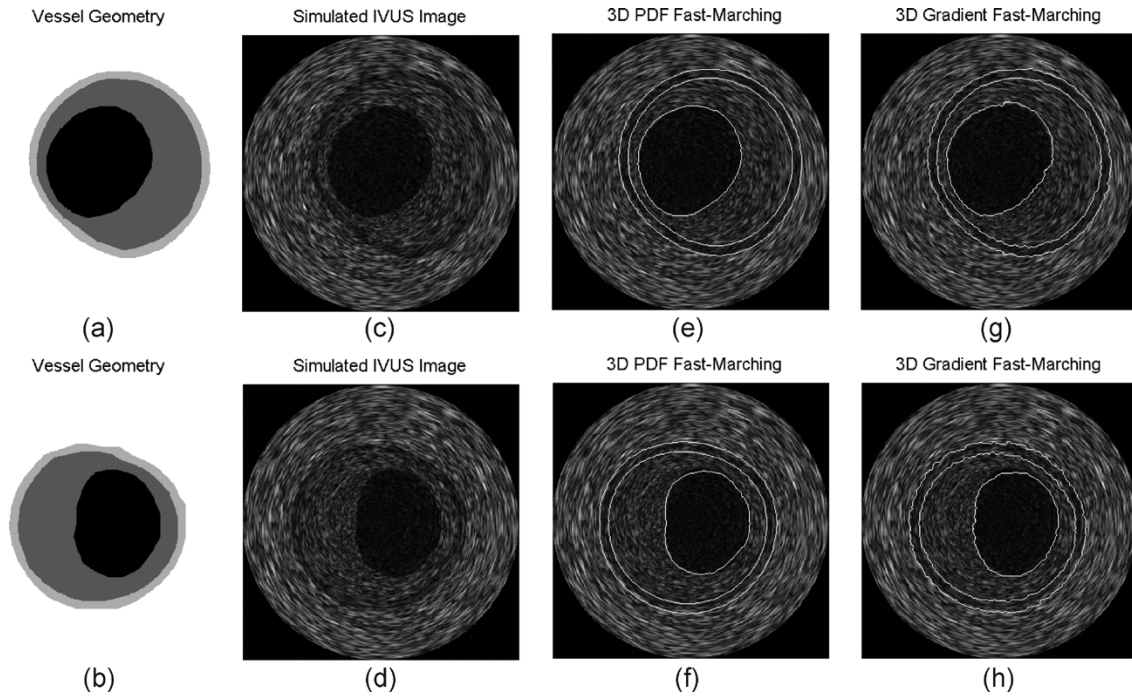


Fig. 5. Segmentation examples on simulated data. (a) and (b) Vessel geometries and (c) and (d) simulated IVUS cross-sectional images. Lumen, thickened intima, and media detected boundaries with (e) and (f) PDFs and (g) and (h) gradient 3-D fast-marching methods.

TABLE III
AVERAGE DISTANCE AND HAUSDORFF DISTANCE BETWEEN DETECTED BOUNDARIES ON SIMULATED IVUS DATA AND TRUE BORDER POSITION

Segmentation Method	Lumen				Plaque				Media			
	AD (mm)		HD (mm)		AD (mm)		HD (mm)		AD (mm)		HD (mm)	
FMM-3D PDFs	0.072±	0.062	0.226±	0.074	0.061±	0.038	0.154±	0.046 *	0.063±	0.038	0.164±	0.048 §
FMM-3D Gradient	0.069±	0.056 §	0.197±	0.085 §	0.060±	0.044	0.173±	0.050	0.063±	0.044	0.180±	0.052

AD is the average distance between the detected boundary and true border, HD is the Hausdorff distance (maximum distance between the boundary and true border). The pixel size is $26 \times 26 \mu\text{m}^2$. FMM-3D is the three-dimensional fast-marching segmentation. PDF signifies probability density function. *, § indicate statistically significant better performance (smaller distances) (* has $p < 0.05$, § has $p < 0.01$ on paired t-test). A column without *, § indicates no statistical difference ($p > 0.05$).

(10) were higher in the lumen region. The lower speeds in the plaque region indicated that the lumen front would propagate slower there.

To evaluate the error of the segmentation method, detected boundaries were compared to manually traced lumen and media contours in Table IV. Small average distances, between 0.12 and 0.16 mm, and Hausdorff distances, between 0.31 and 0.40 mm, were obtained with the PDF- and gradient-based 3-D fast-marching. Only the media Hausdorff distances between these contours, for both PDF and gradient methods, were significantly higher than the interuser variability ($p < 0.05$). This shows that the segmentation errors were smaller than the differences between different manual analyses. Also, the intrauser variability was significantly higher than the segmentation errors for the area measurements ($p < 0.05$). The difference with the manual and 3-D fast-marching boundary areas ranged from -0.2 to 0.4 mm^2 . Area differences do not directly depict point-to-point contour differences, but area measurements are widely used in clinic to evaluate the plaque volume and percentage of stenosis. Area differences between detected and manually segmented contours shown in Table IV were slightly higher than those reported in [16], [18] (between -0.14 ± 1.01 and $0.27 \pm 0.49 \text{ mm}^2$), however, in the current

study, data were acquired on femoral arteries, which are larger than the coronary arteries of these other studies.

Multiple pairwise comparisons with Bonferonni tests were also performed to compare the accuracy of the PDF- and gradient-based segmentation results of Table IV. For the media boundary, smaller Hausdorff distances were obtained with the PDF-based segmentation, but average distances were smaller with the gradient method ($p < 0.05$). The lumen boundary, which often has strong edges, was closer to the manual segmentation with the gradient fast-marching according to the average distances and area differences ($p < 0.05$). However, the difference between the segmentation errors of the gradient and PDF methods were lower than half the pixel size for all point-to-point contour distances. Overall, good performances were achieved with the gradient and the PDF information when used separately in a 3-D fast-marching segmentation scheme. Consequently, it would be interesting to combine these two features in the speed function of (10). Also, the usage of edge direction information could improve the vessel boundary detection in a fast-marching model combining PDF and edge features.

Quantitative evaluation and comparison of the variability or consistency of 3-D fast-marching under different initializations

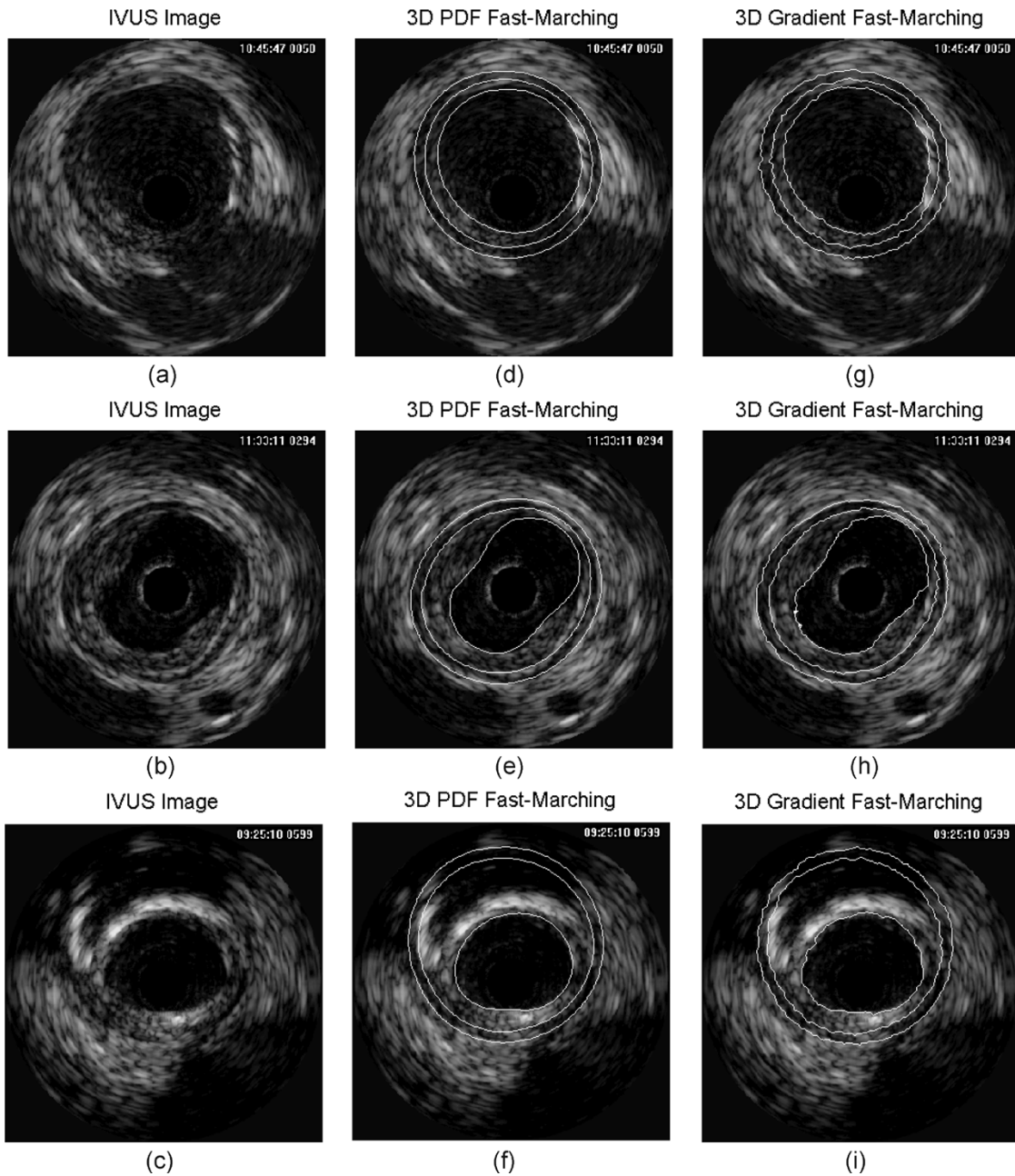


Fig. 6. (a)-(c) Typical IVUS cross-sectional images and corresponding segmentation results. Lumen, thickened intima, and media detected boundaries with (d)-(f) PDFs and (g)-(i) gradient 3-D fast-marching methods.

were performed in Table V with *in vivo* data. Results indicated that PDF-based fast-marching had the smallest Hausdorff distances ($p < 0.01$), which remained under 0.249 mm for all boundaries compared to a value of up to 0.297 mm for the gradient implementation. PDF fast-marching also had relatively small average distances between borders, of 0.083 mm and lower which is less than 3.2 pixels, but they were significantly higher than media average distances obtained with the gradient-based method ($p < 0.05$). However, the differences between these distances were small (lower than the pixel size). Thus, 3-D fast-marching detected boundaries had small variations when initialized differently and the maximum distance to the closest point, representing the worst case, stayed low.

Overall, these results indicate, with small average and Hausdorff distances in Tables IV and V, that the segmentation is accurate even in regions lacking information, for example if desired boundaries were covered by catheter ring-down artifacts, lost behind calcium deposits or in side branches. This is explained by the initial longitudinal contour information, but also by the multiple interface extension of the fast-marching method. The parallel segmentation of the different wall components integrates high-level information because the layered structure of the vessel wall is preserved during the segmentation. Also, because of their associated low speeds, regions of missing speckle information are segmented after all other propagation areas have been explored through the arrival time construction map algorithm based on (9). In these regions, the interfaces are pulled by

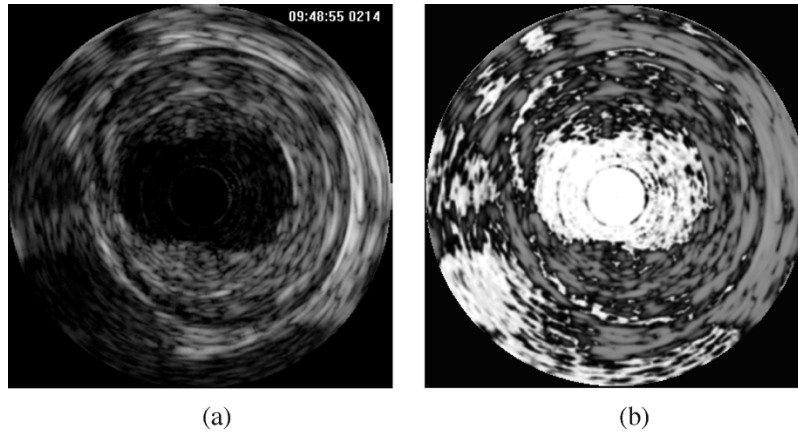


Fig. 7. (a) Typical IVUS cross-sectional image and (b) corresponding speed function map for the lumen interface calculated according to (10) where darker pixels depict lower speed values.

TABLE IV
AVERAGE DISTANCE, HAUSDORFF DISTANCE AND AREA CORRELATION COEFFICIENT BETWEEN DETECTED BOUNDARIES AND MANUAL SEGMENTATION WITH 3-D FAST-MARCHING

Segmentation Method	Lumen					Media				
	AD (mm)		HD (mm)		Area diff (mm ²)	AD (mm)		HD (mm)		Area diff (mm ²)
FMM-3D PDFs	0.16±	0.10*	0.40±	0.25*	0.4± 2.1 (r=0.93)**	0.13±	0.07*	0.31±	0.16§	-0.2± 2.1 (r=0.92)**
FMM-3D Gradient	0.14±	0.10*§	0.39±	0.24*	0.1± 2.0 (r=0.94)**§	0.12±	0.07*§	0.33±	0.16	-0.2± 2.1 (r=0.93)**
Inter-user var	0.18±	0.23	0.44±	0.41	0.6± 2.8 (r=0.89)	0.17±	0.22	0.29±	0.24	0.3± 2.2 (r=0.92)
Intra-user var	0.14±	0.20	0.36±	0.37	0.8± 2.5 (r=0.91)	0.10±	0.08	0.26±	0.21	0.1± 1.9 (r=0.94)

AD is the average distance between manually traced and detected boundaries, HD is the Hausdorff distance (maximum distance between boundaries), Area diff is the difference between the detected and manual contour areas and r is the area correlation coefficient. The pixel size is $26 \times 26 \mu\text{m}^2$. FMM-3D is the three-dimensional fast-marching segmentation. PDF signifies probability density function. Inter-user var and Intra-user var are, respectively, the inter-user and intra-user variabilities; the AD, HD, Area diff and r coefficient were calculated between the different manually traced contours. * and § indicate, respectively, statistically significant smaller value than the inter-user and intra-user variabilities ($p < 0.05$ on pairwise comparisons). A column without * or § indicates no statistical difference with the intra- and inter-user variabilities ($p > 0.05$). § indicates statistically significant better performance between the PDF- and gradient-based method (§ have $p < 0.05$ on pairwise comparisons). A column without § indicates no significant difference ($p > 0.05$).

TABLE V
AVERAGE DISTANCE AND HAUSDORFF DISTANCE BETWEEN DETECTED BOUNDARIES FROM DIFFERENT INITIALIZATIONS ON INTRAVASCULAR ULTRASOUND *In Vivo* DATA

Segmentation Method	Lumen				Plaque				Media	
	AD (mm)		HD (mm)		AD (mm)		HD (mm)		AD (mm)	HD (mm)
FMM-3D PDFs	0.083 ±	0.089	0.249 ±	0.145 *	0.064 ±	0.066	0.190 ±	0.104 *	0.079 ±	0.079
FMM-3D Gradient	0.085 ±	0.099	0.297 ±	0.144	0.065 ±	0.068	0.222 ±	0.100	0.076 ±	0.082 *

AD is the average distance between closest points in different detected boundaries, HD is the Hausdorff distance (maximum distance between boundaries). The pixel size is $26 \times 26 \mu\text{m}^2$. FMM-3D is the three-dimensional fast-marching segmentation. PDF signifies probability density function. * indicates statistically significant better performance (smaller distances) (* has $p < 0.001$ on paired t-test). A column without * indicates no statistical difference ($p > 0.05$).

their adjacent parts that propagated in areas containing reliable information.

In short, fast-marching methods explore the object border area in a detailed manner: all pixels are analyzed with respect to all preceding neighbors through the arrival time map construction. Also, since the initial front is inside the region to segment, the interface is forced to go into the boundary direction. The PDF feature, when used in conjunction with an in-depth exploration algorithm such as the fast-marching, compares very well with the widely used gradient and can be a valuable and relevant information for IVUS segmentation.

B. Other Considerations

A fast-marching segmentation algorithm based on an automatically detected mixture of Rayleigh PDFs was presented for IVUS image analysis. This method was able to identify vessel

wall structure in 3-D; however, some limitations can be identified. As many IVUS segmentation techniques, an initial contour was necessary for the PDF and gradient fast-marching. In this study, contours from 3 longitudinal views were sufficient and were manually traced in 4.1 ± 0.8 minutes. For more complex lesions, the user might have to trace contours on more views during the initialization procedure. This is a limitation of the method. However, the number of initial longitudinal contours could be reduced with a correction strategy based on a multi-scale optimization. With this approach, a higher resolution data set is initialized with low resolution segmentation results of the same pullback. If one adopts this strategy, initial contours would only be used for the segmentation of the coarsest data set. Still, results demonstrated that the PDF information was able to characterize the statistics of each component of the vessel wall. This may be useful for the elaboration of an automatic initialization

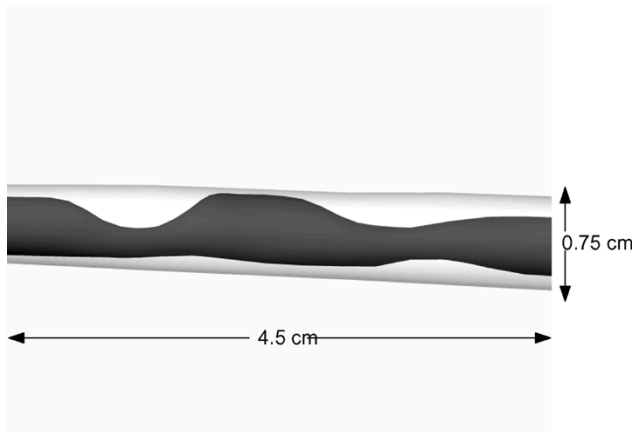


Fig. 8. Example, from one pullback, of the volumetric reconstruction of the lumen (dark gray) and external media boundary (light gray). The 3-D segmentation was performed with the PDF based 3-D fast-marching method (internal media boundary is not shown for better visibility).

strategy, that could be done through a search in likelihood maps of the pixels calculated from the detected mixture.

The processing time for all segmentation calculations (PDF mixture, gradient and 3-D fast-marching) was approximately 1 sec/image for a Matlab and C combined implementation on a Pentium IV 2.6 GHz. Proper data structures were used to handle the arrival time map T to rapidly retrieve, add or remove values. The segmentation was not real-time, however, with some optimizations, close to real-time computation can be expected.

The goal of the PDF parameter estimation is to characterize the statistics of each wall layer over the whole vessel. The EM algorithm was able to estimate a PDF mixture that could fit the IVUS data globally for patients having different vessel wall appearance, even when the pullbacks contained structures such as heterogeneous plaques. For future developments, it is possible to conceive an estimation algorithm that would detect more than four PDFs, in addition to their parameters, to allow the segmentation of the heterogeneous nature of plaques (lipidic, calcified, fibrous, necrotic, etc.). Also, to increase the performance of the proposed segmentation method, other types of PDFs such as the K [34], Nakagami [35] or Rician inverse Gaussian (RiIG) [36] distributions can be considered to model tissues that are not Rayleigh distributed (when the number of scatterers is low, when they are not randomly distributed or when log-compression or other filtering operations performed by the ultrasonic equipment modified the signal PDFs). For these distributions, the cost function of (4) might not be maximized analytically. In this case, to evaluate the mixture parameters, other algorithms such as the stochastic EM [37] might be used. In this study, a Rayleigh PDF mixture was able to model the IVUS gray level distributions.

Finally, for the segmentation of arteries with a small or even absent media, as often seen in the coronary arteries, a weight factor $[\omega_j$ in (2)] close to zero for the media distribution in the PDF mixture estimation is expected. In that case, the segmentation would be performed on the lumen and external vessel boundaries only.

VIII. CONCLUSION

IVUS image processing is a difficult but important task. Image series contain highly relevant clinical information but

are sometimes of poor quality and subject to shadowing and catheter artifacts.

This study has demonstrated the efficiency of fast-marching segmentation using Rayleigh PDF mixture and gradient on *in vivo* and realistic simulation of IVUS images. Fast-marching approach, a segmentation method with small variability, is a promising technique for *in vivo* IVUS image processing. The PDF information is relevant for IVUS image analysis and would benefit of being combined with the gradient information. With an automated initial contour calculation, it is hoped that the fast-marching algorithm using the PDF and/or gradient information may become a reliable segmentation tool of choice for IVUS.

ACKNOWLEDGMENT

The authors would like to thank Z. Qin and I. Renaud for performing the manual segmentations of the IVUS pullbacks.

REFERENCES

- [1] E. J. Gussenhoven, C. E. Essed, C. T. Lancée, F. Mastik, P. Frietman, F. C. van Egmond, J. Reiber, H. Bosch, H. van Urk, J. Roelandt, and N. Bom, "Arterial wall characteristics determined by intravascular ultrasound imaging: an *in vitro* study," *J. Am. Coll. Cardiol.*, vol. 14, no. 4, pp. 947–952, 1989.
- [2] G. S. Mintz, J. A. Painter, A. D. Pichard, K. M. Kent, L. F. Satler, J. J. Popma, Y. C. Chuang, T. A. Bucher, L. E. Sokolowicz, and M. B. Leon, "Atherosclerosis in angiographically 'normal' coronary artery reference segments: an intravascular ultrasound study with clinical correlations," *J. Am. Coll. Cardiol.*, vol. 25, no. 7, pp. 1479–1485, 1995.
- [3] S. Glagov, E. Weisenberg, C. K. Zarins, R. Stankunavicius, and G. J. Kolettsis, "Compensatory enlargement of human atherosclerotic coronary arteries," *New Eng. J. Med.*, vol. 316, no. 22, pp. 1371–1375, 1987.
- [4] A. Colombo, P. Hall, S. Nakamura, Y. Almagor, L. Maiello, G. Martini, A. Gaglione, S. L. Goldberg, and J. M. Tobis, "Intracoronary stenting without anticoagulation accomplished with intravascular ultrasound guidance," *Circulation*, vol. 91, pp. 1676–1688, 1995.
- [5] S. E. Nissen, "Application of intravascular ultrasound to characterize coronary artery disease and assess the progression or regression of atherosclerosis," *Am. J. Cardiol.*, vol. 89, pp. 24B–31B, 2002.
- [6] S. E. Nissen and P. Yock, "Intravascular ultrasound: novel pathophysiological insights and current clinical applications," *Circulation*, vol. 103, pp. 604–616, 2001.
- [7] B. Godbout, J. A. de Guise, G. Soulez, and G. Cloutier, "3D elastic registration of vessel structures from IVUS data on biplane angiography," *Acad. Radiol.*, vol. 12, no. 1, pp. 10–16, 2005.
- [8] A. Wahle, G. P. M. Prause, S. C. DeJong, and M. Sonka, "Geometrically correct 3d reconstruction of intravascular ultrasound images by fusion with biplane angiography methods and validation," *IEEE Trans. Med. Imag.*, vol. 18, no. 8, pp. 686–699, Aug. 1999.
- [9] G. S. Mintz, S. E. Nissen, W. D. Anderson, S. R. Bailey, R. Erbel, P. J. Fitzgerald, F. J. Pinto, K. Rosenfield, R. J. Siegel, E. M. Tuzcu, and P. G. Yock, "American college of cardiology clinical expert consensus document on standards for acquisition, measurement and reporting of intravascular ultrasound studies (IVUS)," *J. Am. Coll. Cardiol.*, vol. 37, no. 5, pp. 1478–1492, 2001.
- [10] J. D. Klingensmith, R. Shekhar, and D. G. Vince, "Evaluation of three-dimensional segmentation algorithms for the identification of luminal and medial-adventitial borders in intravascular ultrasound images," *IEEE Trans. Med. Imag.*, vol. 19, no. 10, pp. 996–1011, Oct. 2000.
- [11] G. Kovalski, R. Beyar, R. Shofti, and H. Azhari, "Three-dimensional automatic quantitative analysis of intravascular ultrasound images," *Ultrasound Med. Biol.*, vol. 26, no. 4, pp. 527–537, 2000.
- [12] X. Zhang, C. R. McKay, and M. Sonka, "Tissue characterization in intravascular ultrasound images," *IEEE Trans. Med. Imag.*, vol. 17, no. 6, pp. 889–899, Dec. 1998.
- [13] C. von Birgelen, C. D. Mario, W. Li, J. C. H. Schuurbijs, C. J. Slager, P. J. de Feyter, P. W. Serruys, and J. R. T. C. Roelandt, "Morphometric analysis in three-dimensional intracoronary ultrasound: an *in vitro* and *in vivo* study using a novel system for the contour detection of lumen and plaque," *Am. Heart J.*, vol. 132, no. 2, pp. 516–527, 1996.

- [14] A. Mojsilovic, M. Popovic, N. Amodaj, R. Babic, and M. Ostojic, "Automatic segmentation of intravascular ultrasound images: a texture-based approach," *Ann. Biomed. Eng.*, vol. 25, no. 6, pp. 1059–1071, 1997.
- [15] C. Haas, H. Ermert, S. Holt, P. Grewe, A. Machraoui, and J. Barmeyer, "Segmentation of 3D intravascular ultrasonic images based on a random field model," *Ultrasound Med. Biol.*, vol. 26, no. 2, pp. 297–306, 2000.
- [16] G. Koning, J. Dijkstra, C. von Birgelen, J. C. Tuinenburg, J. Brunette, J.-C. Tardif, P. W. Oemrawsingh, C. Sieling, S. Melsa, and J. H. C. Reiber, "Advanced contour detection for three-dimensional intracoronary ultrasound: a validation—in vitro and in vivo," *Int. J. Cardiac Imag.*, vol. 18, pp. 235–248, 2002.
- [17] F. Weichert, H. Müller, U. Quast, A. Kraushaar, P. Spilles, M. Heintz, C. Wilke, C. von Birgelen, R. Erbel, and D. Wegener, "Virtual 3D IVUS model for intravascular brachytherapy planning. 3D segmentation, reconstruction, and visualization of coronary artery architecture and orientation," *Med. Phys.*, vol. 30, no. 9, pp. 2530–2536, 2003.
- [18] E. G. P. Bovenkamp, J. Dijkstra, J. G. Bosch, and J. H. C. Reiber, "Multi-agent segmentation of IVUS images," *Pattern Recognit.*, vol. 37, pp. 647–663, 2004.
- [19] E. Brusseau, C. L. de Korte, F. Mastik, J. Schaar, and A. F. W. van der Steen, "Fully automatic luminal contour segmentation in intracoronary ultrasound imaging—a statistical approach," *IEEE Trans. Med. Imag.*, vol. 23, no. 5, pp. 554–566, May 2004.
- [20] C. B. Burckhardt, "Speckle in ultrasound b-mode scans," *IEEE Trans. Son. Ultrason.*, vol. SU-25, no. 1, pp. 1–6, 1978.
- [21] R. F. Wagner, S. W. Smith, J. M. Sandrik, and H. Lopez, "Statistics of speckle in ultrasound B-scans," *IEEE Trans. Sonics Ultrason.*, vol. 30, no. 3, pp. 156–163, 1983.
- [22] J. A. Sethian, *Level Set Methods and Fast Marching Methods. Evolving Interfaces in Computational Geometry, Fluids Mechanics, Computer Vision and Materials Science*, 2nd ed. Cambridge, U.K.: Cambridge Univ. Press, 1999.
- [23] M.-H. Roy Cardinal, J. Meunier, G. Soulez, E. Thérasse, and G. Cloutier, "Intravascular ultrasound image segmentation: a fast-marching method," in *Lecture Notes in Computer Science*. Berlin, Germany: Springer-Verlag, 2003, vol. 2879, Proc. MICCAI 2003: Medical Image Computing & Computer Assisted Intervention, pp. 432–439.
- [24] A. P. Dempster, N. M. Laird, and D. B. Rubin, "Maximum likelihood from incomplete data via the EM algorithm," *J. Roy. Statist. Soc. B*, vol. 39, no. 1, pp. 1–38, 1977.
- [25] S. Osher and J. A. Sethian, "Fronts propagating with curvature-dependent speed: algorithms based on Hamilton-Jacobi formulations," *J. Comput. Phys.*, vol. 79, pp. 12–49, 1988.
- [26] R. Malladi, J. A. Sethian, and B. C. Vemuri, "Shape modeling with front propagation: a level set approach," *IEEE Trans. Pattern Anal. Mach. Intell.*, vol. 17, no. 2, pp. 158–175, Feb. 1995.
- [27] J. A. Sethian, "A fast marching level set method for monotonically advancing fronts," *Proc. Nat. Acad. Sci.*, vol. 93, pp. 1591–1595, 1996.
- [28] J. N. Tsitsiklis, "Efficient algorithms for globally optimal trajectories," *IEEE Trans. Automat. Contr.*, vol. 40, no. 9, pp. 1528–1538, Sep. 1995.
- [29] E. Sifakis, C. Garcia, and G. Tziritas, "Bayesian level sets for image segmentation," *J. Vis. Commun. Image Representation*, vol. 13, pp. 44–64, 2002.
- [30] J. L. Juergens, J. A. Spittell, J. F. Fairbairn, E. van Nuys Allen, N. W. Barker, and E. A. Hines, *Peripheral Vascular Diseases*, 5th ed. Philadelphia, London, Toronto: W. B. Saunders Company, 1980.
- [31] V. Chalana and Y. Kim, "A methodology for evaluation of boundary detection algorithms on medical images," *IEEE Trans. Med. Imag.*, vol. 16, no. 5, pp. 642–652, Oct. 1997.
- [32] R. L. Maurice, J. Ohayon, G. Finet, and G. Cloutier, "Adaptating the Lagrangian speckle model estimator for endovascular elastography: theory and validation with simulated radio-frequency data," *J. Acoust. Soc. Am.*, vol. 116, no. 2, pp. 1276–1286, 2004.
- [33] F. Kallel, M. Bertrand, and J. Meunier, "Speckle motion artifact under tissue rotation," *IEEE Trans. Ultrason., Ferroelect., Freq. Contr.*, vol. 41, no. 1, pp. 105–122, Jan. 1994.
- [34] V. Dutt and J. F. Greenleaf, "Statistics of the log-compressed echo envelope," *J. Acoust. Soc. Am.*, vol. 99, no. 6, pp. 3817–3825, 1996.
- [35] P. M. Shankar, "A general statistical model for ultrasonic backscattering from tissues," *IEEE Trans. Ultrason., Ferroelect., Freq. Contr.*, vol. 47, no. 3, pp. 727–736, Mar. 2000.
- [36] T. Eltoft, "The rician inverse Gaussian distribution: a new model for nonrayleigh signal amplitude statistics," *IEEE Trans. Image Process.*, vol. 14, no. 11, pp. 1722–1735, Nov. 2005.
- [37] P. Masson and W. Pieczynski, "SEM algorithm and unsupervised statistical segmentation of satellite images," *IEEE Trans. Geosci. Remote Sens.*, vol. 34, pp. 618–633, May 1993.